Joint Research Highlights

Conductivity Switching by Reversible Electric-Field-Induced Proton Transfer for a Hydrogen-Bonding Heterobilayer Film

Heteromolecular interactions are responsible for a variety of functions. We reported the first observation of reversible tunneling conductivity switching induced by external electric field (EEF) for a proton (H^+) donor/acceptor bilayer film on Au substrates under ambient conditions at room temperature [1].

Depending on the H^+-transferred sites, the molecular orbitals of the H^+-donor and -acceptor molecules are modified. Thus, the H^+-transfer in the heteromolecular pair is able to control molecular properties and to function as a switch. To achieve this function in molecular systems, catechol-fused tetrathiafulvalene (Cat-TTF) derivatives were introduced, which were designed to exhibit H^+-electron-correlated properties [2-4]. We fabricated the bilayer films containing Cat-TTF derivatives as a H^+-donor and imidazole-terminated undecanethiolate self-assembled monolayer (Im-SAM) as a H^+-acceptor on Au substrates (Fig. 1a), through a two-step immersion procedure. The bilayer film topographies, molecular adsorption states, and physical properties were characterized using several spectroscopic and microscopic methods.

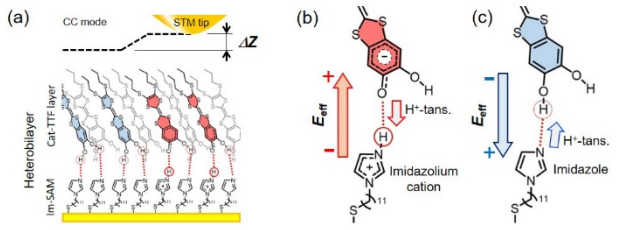

Fig. 1. Schematic of Cat-TTF/Im-SAM bilayer film and EEF response in STM measurements under CC mode (a), H^+-transfer from a catechol moiety to an imidazole group (b), and its reverse H^+-transfer (c), depending on EEF.

In particular, scanning tunneling microscope (STM) revealed reversible changes in the tunneling conductivity of the bilayer film depending on EEF stimulation. Figure 2a shows a typical STM image of the bilayer film, obtained in constant current (CC) mode. The observed atomically flat terraces and steps imply that the bilayer film is uniform in terms of structurally and quantum tunneling properties. Figures 2b–2d show STM images of the bilayer film after EEF stimulation at various stimulation sample-bias V_{SS}. At negative V_{SS} (-1.5 V), the stimulated area surrounded by red corners in Fig. 2b increased in height change ($\Delta Z > 0$), implying increase of tunneling conductivity. This applied EEF may transfer H^+ from the catechol moiety to the imidazole group in the bilayer film (Fig. 1b). In contrast, at the stimulation by positive V_{SS} (+2.0 V) to a part of high conductivity area, surrounded by light-blue corners in Fig. 2c, the area returned to original height ($\Delta Z \approx 0$). This EEF may transfer H^+ from the imidazole group back to the catechol moiety (Fig. 1c). Moreover, the area surrounded by red corners in Fig. 2d increased in height again by negative V_{SS} (-1.5 V). We confirmed that this height change in the CC mode is corresponding to the conductivity change by a *di/dv* mapping method. The mechanism of reversible conductivity switching is considered to be H^+-transfer by applied EEF. The ability of H^+-transfer under EEF was theoretically expected in molecular cluster calculations.

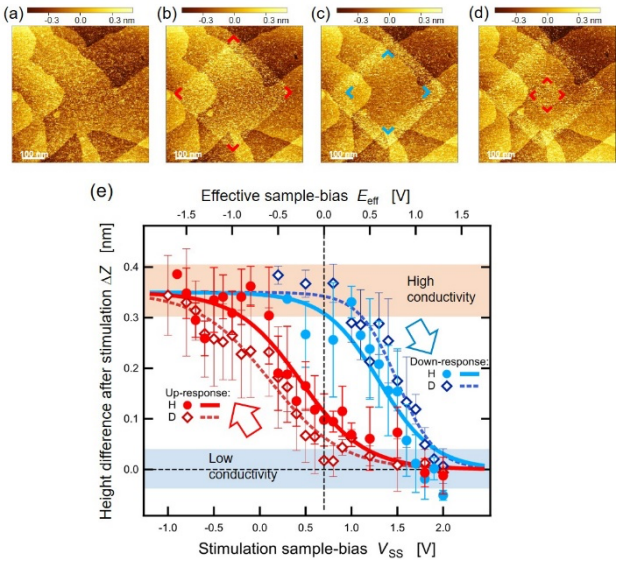

Fig. 2. STM topographies of the bilayer film before (a) and after EEF stimulation at sample bias V_{SS} = -1.5 V (b), +2.0 V (c), and -1.5 V (d). The height change ΔZ against V_{SS} is shown in (e) including its H/D isotope dependence. All measurements were performed in air at room temperature.

Figure 2e shows the EEF-induced height change ΔZ against V_{SS}. These results clearly demonstrate two important features: the threshold of the EEF response exhibits hysteresis and H/D isotope dependence. The isotope dependence is crucial evidence of the EEF response due to H^+-transfer. In addition, the hysteresis in the EEF response indicates that the bilayer film can function as a molecular memory device driven by the H^+-transfer.

References

[1] H. S. Kato *et al.*, Nano. Lett. **25**, 11116 (2025).
[2] T. Isono *et al.*, Nat. Commun. **4**, 1344 (2013).
[3] A. Ueda *et al.*, J. Am. Chem. Soc. **136**, 12184 (2014).
[4] H. Mori *et al.*, Chem. Commun. **22**, 5668 (2022).

Authors

H. S. Kato[a], R. Muneyasu[a], T. Fujino[b], A. Ueda[c], Y. Kanematsu[d], M. Tachikawa[e], J. Yoshinobu, and H. Mori
[a]Osaka University
[b]Yokohama National University
[c]Kumamoto University
[d]Hiroshima University
[e]Yokohama City University

PI of Joint-use project: H. S. Kato
Host labs: Mori and Yoshinobu Groups

Rotational Grüneisen Ratio as a Novel Probe for Quantum Criticality in Anisotropic Systems

Quantum criticality, a phenomenon driven by quantum fluctuations near absolute zero, plays a pivotal role in understanding exotic states in condensed matter systems. In this study [1], we introduce a novel thermodynamic quantity, the rotational Grüneisen ratio Γ_ϕ, as a highly sensitive probe for detecting quantum critical behavior in anisotropic systems.

The rotational Grüneisen ratio Γ_ϕ is defined as $\Gamma_\phi = (1/T)(\partial T/\partial\phi)_S$, where ϕ is the angle of the external field. In contrast to conventional Grüneisen parameters, which employ the *magnitude* of the magnetic field or pressure as control parameters, the rotational Grüneisen ratio utilizes the *angle* ϕ of the external field as a tuning parameter. This method enables the detection of quantum phase transitions with higher angular resolution by measuring the rotational magnetocaloric effect, $(\partial T/\partial\phi)_S$ [2].

We applied this method to two highly anisotropic paramagnets, CeRhSn and CeIrSn, both of which possess a quasi-kagome lattice and exhibit strong geometrical frustration and Kondo effect. By measuring the rotational magnetocaloric effect under varying a magnetic field angle within the ac plane, we investigated Γ_ϕ over a wide range of temperatures, magnetic fields, and field orientations.

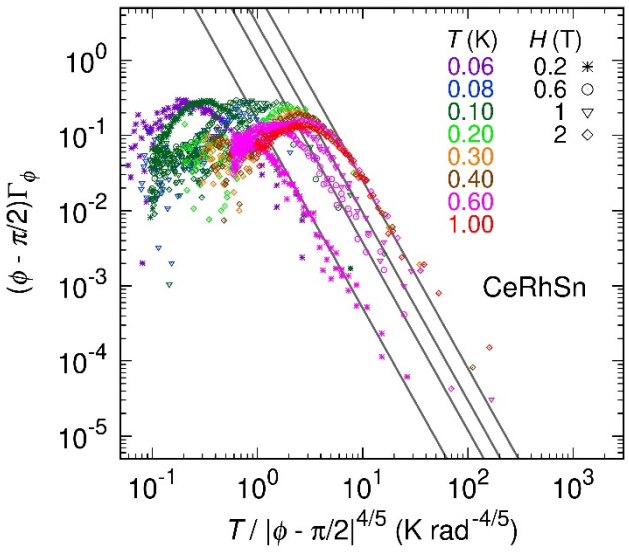

Fig. 1. Scaling plot of the rotational Grüneisen ratio Γ_ϕ for CeRhSn for various temperatures and several selected magnetic fields. Solid lines indicate the scaling functions.

Remarkably, for both compounds, the $(\phi - \phi_{cr})\Gamma_\phi$ data at each magnetic field collapse onto a universal scaling function $f(T/(\phi - \phi_{cr})^n)$, with identical critical exponents $n = 4/5$ and a critical field angle $\phi_{cr} = \pi/2$, as exemplified in Fig. 1 for CeRhSn. These results indicate the existence of a quantum critical line along the hard-magnetization axis (the a axis), where the c-axis component of the magnetic field, $H_\parallel$, governs the critical behavior. The scaling behavior of the rotational magnetic Grüneisen ratio, $\tilde{\Gamma}_\phi = -\Gamma_\phi/H_\perp$, further supports the universality of the quantum criticality, where $H_\perp$ denotes the a-axis component of the magnetic field. The constant $H_\parallel\tilde{\Gamma}_\phi$ supports the presence of a quantum critical point at $H_\parallel = 0$. The small value of the critical exponent implies relatively long correlation length and time, potentially reflecting a characteristic feature of quantum criticality driven by geometrical frustration in these compounds.

These findings highlight that the rotational Grüneisen ratio as a powerful and versatile tool for investigating quantum criticality in strongly anisotropic systems, such as Ising magnets. This method enables high-resolution, field-angle-resolved measurements, providing a novel approach to exploring quantum phase transitions in anisotropic materials.

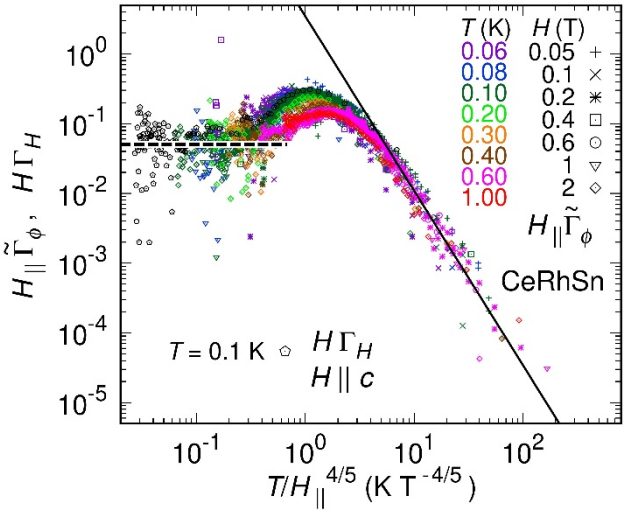

Fig. 2. Scaling plots of the rotational magnetic Grüneisen ratio $\tilde{\Gamma}_\phi$ and magnetic Grüneisen ratio Γ_H for CeRhSn. The solid line indicates the universal scaling function $\tilde{\Gamma}_\phi \sim H_\parallel T^{-5/2}$. The dashed line represents $H_\parallel\tilde{\Gamma}_\phi = 0.05$.

References

[1] S. Yuasa *et al.*, Phys. Rev. B **111**, 045123 (2025).
[2] S. Kittaka *et al.*, J. Phys. Soc. Jpn. **87**, 073601 (2018).

Authors

S. Yuasa[a], Y. Kono[a], Y. Ozaki[a], M. Yamashita, Y. Shimura[b], T. Takabatake[b], and S. Kittaka[a,c]
[a]Chuo University
[b]Hiroshima University
[c]Department of Basic Science, The University of Tokyo

PI of Joint-use project: S. Kittaka
Host lab: Yamashita Group

Polarity of Homoepitaxial ZnO Films

ZnO is an oxide semiconductor that has been shown to be a useful optoelectronic material due to the wide tunability of the direct band gap from 3 to 4.4 eV by Mg or Cd doping. In practical device applications, the device characteristics are strongly influenced by the polarity direction of the crystal, i.e., whether the wurtzite-type crystal is terminated by a zinc face or an oxygen face. For perfect epitaxial thin film layers, the crystal polarity is determined by the termination of the underlying layer. In practical films, however, the film termination can change, depending on the film growth conditions. When grown on an $Al_2O_3(0001)$ surface, ZnO films tend to be terminated by the zinc face when grown at a slow rate at high temperature. The termination switches to the oxygen face at high growth rates or low growth temperatures.

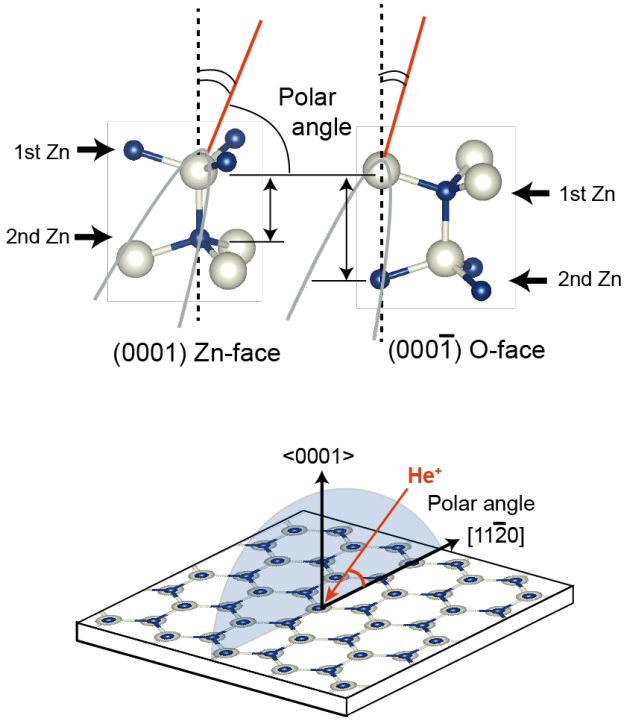

Fig. 1. He ion backscattering geometries for the two ZnO terminations and the CAICISS measurement geometry.

In this work [1], we have used co-axial impact-collision ion scattering spectroscopy (CAICISS) to determine the termination type of homoepitaxial ZnO films grown by Nd:YAG laser ablation at various growth conditions. CAICISS can be used to determine the crystal polarity by measuring the angle dependence of backscattered He ions from a crystal surface. The measurement geometry and the crystal polarity models are shown in Fig. 1. For ZnO structure analysis, the time-of-flight window is set at He ion backscattering from Zn atoms. The scattering is angle dependent, mostly due to He ion focusing and shadowing that occurs in the two topmost atomic layers. High backscattering intensity is observed at slightly different polar angles for the Zn- and O-face crystal terminations.

Homoepitaxial Mg:ZnO films were grown at several temperatures to verify if a termination change occurs similarly to growth on $Al_2O_3(0001)$. Although there were significant surface morphology differences, the CAICISS polar scans were essentially unchanged. The optimal growth temperature for surface flatness was found to be 550 °C at an oxygen pressure of 10^{-5} Torr. The films were grown by pulsed laser deposition (PLD) with a fourth-harmonic Nd:YAG laser operating at 10 Hz and an ablation fluence of 2.3 J/cm^2.

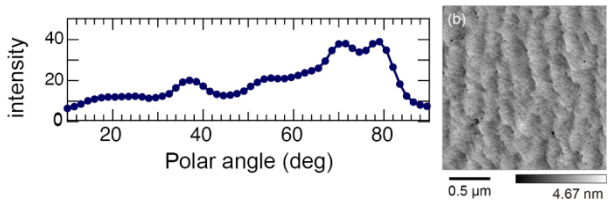

Fig. 2. Polar angle dependence of He ion scattering intensity from Zn atoms (left) and an AFM image of the film surface morphology (right).

The polar angle ion scattering scan is shown in Fig. 2 together with an atomic force microscope (AFM) topography image. The double peak structure in the ion scattering intensity between 70 and 80 degrees indicates the presence of the ZnO oxygen face, same as the substrate surface.

These results show that it is possible to use solid-state laser pulsed laser deposition to fabricate ZnO films with a clear step-and-terrace morphology while maintaining a constant ZnO layer termination.

References

[1] T. Masuda, T. Sato, M. Lippmaa, T. Dazai, N. Sekine, I. Hosako, H. Koinuma and R. Takahashi, J. Appl. Phys. 136, 095303 (2024).

Authors

T. Masuda[a], T. Sato[b], M. Lippmaa, T. Dazai[c], N. Sekine[d], I. Hosako[d], H. Koinuma[a], and R. Takahashi[c]
[a]Smart Combinatorial Technology, Inc.
[b]Vacuum Products, Inc.
[c]Nihon University
[d]NICT

PI of Joint-use project: R. Takahashi
Host lab: Lippmaa Group

Observation of Current-Induced Lattice Distortion in Spin–Orbit Coupled Iridium Oxide $Ca_5Ir_3O_{12}$

Recently, a nonlinear electrical conductivity has been reported in single crystals of 4*d* and 5*d* transition metal (TM) oxides. In the layered perovskite oxides Ca_2RuO_4 and Sr_2IrO_4, conductivity is increased when current is applied and nonlinear electrical conductivity is observed [1–3]. In the layered structure, the TM–O–TM bond angle, which is important for conductivity, is changed by the application of current. It has been reported that the crystal structure of these materials under the application of current is in a non-equilibrium state, which is different from the thermal equilibrium state. Spin–orbit coupling is thought to play an important role in the nonlinear electrical conductivity of these 4*d* and 5*d* transition metal oxides. Therefore, such spin–orbit coupled materials are expected to have applications in devices based on a new mechanism.

We have reported that $Ca_5Ir_3O_{12}$ exhibits nonlinear electrical conductivity along the *c*-axis [4,5]. $Ca_5Ir_3O_{12}$ has a hexagonal crystal structure without centrosymmetry, in which one-dimensional chains of edge-sharing IrO_6 octahedra along the *c*-axis form triangular lattices in the *c*-plane (Fig. 1). Recently, to investigate the effect of current application on the crystal structure, Raman scattering experiments on $Ca_5Ir_3O_{12}$ were performed under the application of DC current [6]. Changes in the Raman spectrum caused by the application of DC current, which are different from the effect of self-heating due to DC current, were also observed. These results indicate that the oxygen bonds in the edge-sharing IrO_6 chain along the *c*-axis are strengthened by applying a DC current.

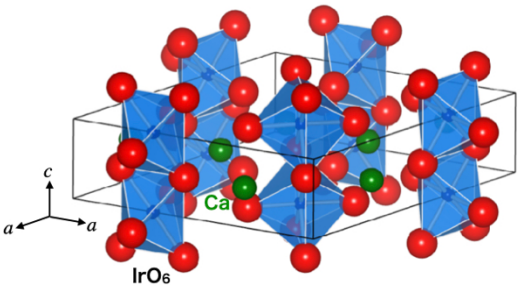

Fig. 1. Crystal structure of $Ca_5Ir_3O_{12}$.

In this study, we report current-induced lattice distortion in iridium oxide $Ca_5Ir_3O_{12}$ with a hexagonal structure that exhibits nonlinear conductivity along the *c*-axis [7]. Using the synchrotron radiation X-ray diffraction experiments on the single crystal, the change in the lattice constant due to thermal expansion at temperatures above room temperature and the change in the lattice constant due to the application of current along the *c*-axis were investigated. We found that the current application along the *c*-axis caused anisotropic lattice distortion that expanded within the *c*-plane direction. The observed distortion due to the electric current is not caused by the piezoelectric effect that would be expected given the symmetry of the crystal structure of this material; the evaluated piezoelectric constant is a very large value compared to typical piezoelectric materials. These results show that the change in the lattice constant ratio *a*/*c* due to the application of current is greater than the change in thermal expansion caused by self-heating. In spin–orbit coupled oxides, this result reveals the possibility of significant current-induced distortion based on a mechanism different from the conventional piezoelectric effect.

References

[1] G. Cao, J. Phys.: Condens. Matter **32**, 423001 (2020).
[2] R. Okazaki, Y. Nishina, Y. Yasui, F. Nakamura, T. Suzuki, and I. Terasaki, J. Phys. Soc. Jpn. **82**, 103702 (2013).
[3] G. Cao, J. Terzic, H. D. Zhao, H. Zheng, L. E. De Long, and P. S. Riseborough, Phys. Rev. Lett. **120**, 017201 (2018).
[4] K. Matsuhira, K. Nakamura, Y. Yasukuni, Y. Yoshimoto, D. Hirai, and Z. Hiroi, J. Phys. Soc. Jpn. **87**, 013703 (2018).
[5] H. Hanate, K. Nakamura, and K. Matsuhira, J. Magn. Magn. Mater. **498**, 166203 (2020).
[6] M. Hayashida, T. Hasegawa, K. Kadohiro, H. Hanate, S. Kawano, and K. Matsuhira, J. Phys. Soc. Jpn. **93**, 104704 (2024).
[7] K. Kadohiro, H. Hanate, M. Hayashida, T. Hasegawa, H. Nakao, Y. Okamoto, K. Miyazaki, S. Tsutsui, and K. Matsuhira, J. Phys. Soc. Jpn. **94**, 023601 (2025).

Authors

K. Matsuhira[a] and Y. Okamoto
[a]Kyushu Institute of Technology

PI of Joint-use project: K. Matsuhira
Host lab: Okamoto Group, Materials Synthesis Section

Development of Open Data Analysis Tool for Science and Engineering (ODAT-SE)

We developed open-source software Open Data Analysis Tool for Science and Engineering (ODAT-SE) [1], by the PASUMS project in FY2024 as a major upgrade of 2DMAT [2, 3]. ODAT-SE solves an inverse problem, when one gives a direct or forward model, a physical or statistical model representing the system under investigation. Currently, ODAT-SE offers five analysis methods: (i) grid search, (ii) Nelder-Mead optimization, (iii) Bayesian optimization, (iv) replica exchange Monte Carlo method, and (v) population-annealing Monte Carlo (PAMC) method.

The code structure of ODAT-SE is drawn schematically in Fig. 1. The original architecture in 2DMAT was tightly coupled with specific experimental techniques, limiting its flexibility and reusability across other scientific fields. In ODAT-SE, the architecture explicitly separates direct problems from the optimization or search algorithms. This modular approach enables researchers to apply ODAT-SE to diverse fields; users can easily add their own direct problem solvers or search algorithms tailored to their research needs.

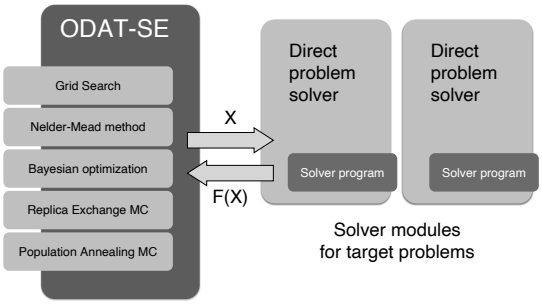

Fig. 1. Schematic diagram of the code structure of ODAT-SE.

Hereafter, we focus on the PAMC method, a massively parallel Bayesian inference. In general, the Bayesian inference gives the posterior probability distribution $P(X|Y)$, as histogram, where X is the target quantity (vector), the quantity that we would like to know, and Y is the experimentally observed quantity (vector). The PAMC method is suitable to supercomputers. Since the PAMC method is a global search algorithm, one can find the global solution and local solutions in the data space of X. The PAMC method was used to determine the surface structure of the 3×3-Si phase on the Al (111) surface by total reflection high-energy positron diffraction experiment (https://www2.kek.jp/imss/spf/eng/, Fig. 2(a)) and core-level photoemission spectroscopy [4]. The analysis finds the global solution as a flat surface structure shown in Fig. 2(b) and local solutions, which indicates the crucial importance of global search algorithm.

In future outlook, ODAT-SE will be developed further and used both in plasma and material science, for example, through our project launched recently in the Moonshot R&D Program [5]. Notably, a recent study [6] using 2DMAT have successfully demonstrated efficient fitting of high-dimensional experimental parameters. With the modular architecture of ODAT-SE, similar complex analyses can now be performed more easily, enabling broader applicability across various scientific fields.

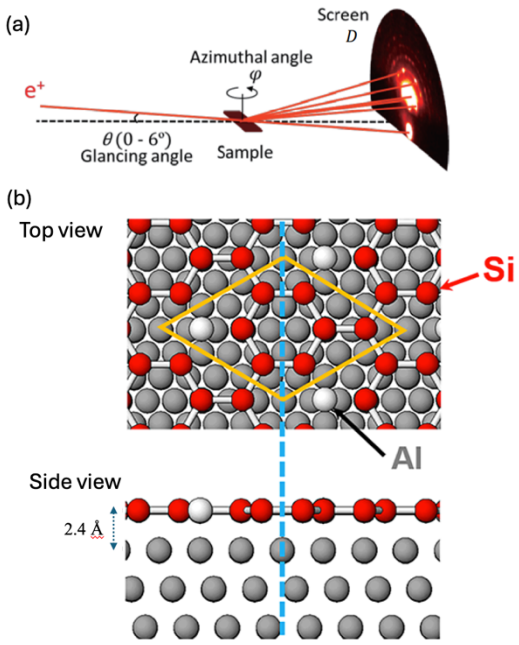

Fig. 2. (a) Schematic diagram of total reflection high-energy positron diffraction experiment (b) Top view (upper panel) and side view (lower panel) for the surface structure of the 3×3-Si phase on the Al (111) surface [4].

References

[1] https://www.pasums.issp.u-tokyo.ac.jp/odat-se/
[2] Y. Motoyama *et al*., Comp. Phys. Commun. **280**, 108465 (2022).
[3] https://www.pasums.issp.u-tokyo.ac.jp/2dmat/
[4] Y. Sato *et al*., Phys. Rev. Materials **9**, 014002 (2025).
[5] https://www.jst.go.jp/moonshot/en/program/goal10/A3_hoshi.html
[6] S. Liu *et al*., Phys. Rev. Lett. **135**, 056502 (2025).

Authors

T. Hoshi[a,b], A. Nakano[a,b], T. Aoyama, Y. Motoyama, and K. Yoshimi
[a] National Institute for Fusion Science
[b] The Graduate University for Advanced Studies, SOKENDAI

PI of Joint-use project: Takeo Hoshi
Host lab: supercomputer center

Temperature-Dependent Magnetic, Electronic, and Structural Properties of $Ba_2Fe_{14}O_{22}$: Effects of Fe^{2+} Localization

In this study, we conducted a comprehensive investigation of the magnetic, electronic, and structural properties of high-quality polycrystalline Y-type ferrite $Ba_2Fe_{14}O_{22}$ throughout a wide temperature range [1]. This compound with a mixed valence state of Fe^{2+} and Fe^{3+} is expected to display a rich variety of physical phenomena because of the interplay of charge, spin, and orbital degrees of freedom. Previous studies have been impeded by the difficulties in synthesizing phase-pure samples since ferrimagnetic impurities like $BaFe_2O_4$ and Fe_3O_4 can contaminate $Ba_2Fe_{14}O_{22}$. We were able to synthesize high-purity polycrystalline samples that are ideal for studying the material's intrinsic characteristics by fine-tuning solid-state reaction conditions.

A ferrimagnetic transition was detected at 662 K, which is somewhat higher than the values reported in previous literature [2,3], according to magnetic measurements. Dissimilarities in oxygen stoichiometry are probably to blame for this disparity. The finding of a precipitous decrease in magnetization at 160 K points to the existence of a phase transition. The magnetic moment per formula unit drops from 9.4 μ_B before of the transition to 8.8 μ_B below it. Magnetization curves above the transition and below 160 K are also significantly different.

Above the transition, the magnetization curve indicates planar-type collinear ferrimagnetism with saturation occurring at around 20 kOe. In contrast, the magnetization grows ferromagnetically at lower temperatures; it keeps growing linearly all the way up to 70 kOe, though. We can infer a non-collinear magnetic structure from this unsaturated field-linear behavior near high fields.

Electrical conductivity measurements indicate semiconducting behavior with moderate conductivity at room temperature ($\rho \approx 33\ \Omega\cdot$cm). On cooling, conductivity gradually diminishes and shows a drop near 160 K, suggesting carrier localization. The conductivity exhibits Arrhenius-type behavior at lower temperatures, with two distinct activation energies: 98 meV between 105–125 K, and 50 meV below 105 K. This implies a reduction in carrier population and mobility at low temperatures.

Figure 1 illustrates the powder X-ray diffraction pattern obtained using Cu-$K\alpha_1$ radiation on a SmartLab diffractometer with a He closed-cycle refrigerator system. The results revealed a structural phase transition at 160 K from a high-temperature rhombohedral to a low-temperature triclinic crystal system. The site-selective localization of Fe^{2+} ions is thought to be the cause of this structural change. Owing to the larger ionic radius compared to Fe^{3+}, Fe^{2+} ions preferentially occupy octahedral sites, particularly those with an up-spin alignment in the magnetic structure. The magnetic moment per formula unit decreases from 9.4 μ_B above the transition to 8.8 μ_B below it, consistent with the theoretical value assuming Fe^{2+} localization among specific octahedral sites.

In summary, this study elucidates the intrinsic temperature-dependent properties of $Ba_2Fe_{14}O_{22}$ by combining structural, magnetic, and electronic measurements. The first order structural transition at 160 K, linked to Fe^{2+} site-selective localization, leads to a reduction in magnetic moment and a marked change in magnetic anisotropy. These findings highlight the intricate coupling between charge, spin, and lattice degrees of freedom in mixed valence hexaferrites.

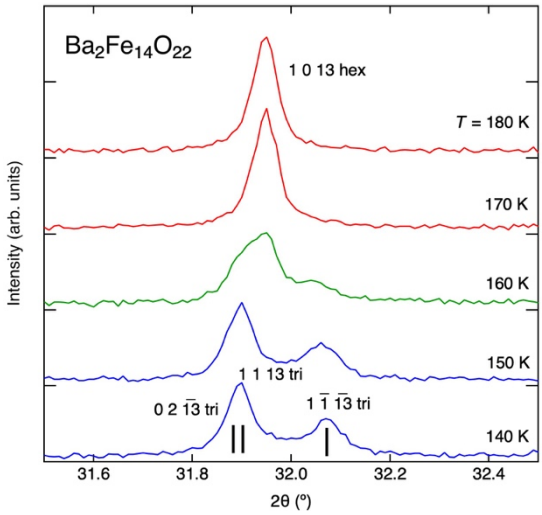

Fig. 1. X-ray diffraction pattern of 1 0 13 reflection (indexed by high-temperature phase manner) near the phase transition at 160 K. The reflection splits into three with the 0 2 -13, 1 1 13, 1 -1 -13 reflections (indexed by low-temperature phase manner).

References

[1] T. Waki *et al*., J. Phys. Soc. Jpn. **94** (in press).
[2] M. A. H. Farhat and J. C. Joubert, J. Magn. Magn. Mater. **62**, 353 (1986).
[3] X. Zhang and J. Zhang, Mater. Lett. **269**, 127642 (2020).

Authors

T. Waki[a], R. Sobajima[a], J. Yamaura, Y. Tabata[a], and H. Nakamura[a]
[a]Department of Materials Science and Engineering, Kyoto University

PI of Joint-use project: Takeshi Waki
Host lab: Yamaura group and X-Ray Diffraction Section

Neutron Scattering Studies on the Room-Temperature Altermagnet FeS

Antiferromagnets with broken time-reversal symmetry, which are also termed altermagnets, have been attracting marked attention in condensed matter physics in recent years [1], because they potentially show emergent phenomena, such as large anomalous Hall effect or spin-current generation, which would be applicable to novel spintronics devices in the future. We have recently discovered a new altermagnet FeS, which exhibits antiferromagnetic (AFM) order and spontaneous Hall effect at room temperature [2]. This system is known to exhibit a spin reorientation transition at around 190 K. We found that the spontaneous Hall effect disappears at this transition. To investigate the magnetic structures above and below the transition temperature, we performed unpolarized and polarized neutron scattering measurements with a single crystal of FeS.

Unpolarized neutron diffraction measurements were carried out at High-Resolution Spectrometer HRC(BL12) in the Materials and Life-science experimental Facility (MLF) in Japan Accelerator Research Complex (J-PARC). A single crystal of FeS was mounted in a closed-cycle ^{4}He refrigerator with the (*H*,*H*,*L*) horizontal scattering plane. The sample was exposed to a pulsed polychromatic incident neutron beam. Bragg reflections from the sample were detected by the ^{3}He position sensitive detectors. Figures 1(a) and 1(b) show the comparison between the temperature variations of magnetic susceptibilities and the integrated intensity of the 002 Bragg reflection, at which nuclear scattering is expected to be very weak. Since the neutron scattering cross section of a magnetic peak is proportional to a square of Fourier-transformed magnetization projected onto the plane perpendicular to the scattering vector, the intensity of the 002 reflection at high temperatures is attributed to the easy-plane type q=0 AFM structure as illustrated in the inset on the right side of Fig. 1b. At around 190 K, the intensity of the 002 reflection was abruptly reduced, which is exactly coincides with the sharp drop of the magnetic susceptibility along the *c* axis. These changes can be interpreted that the system undergoes the spin-reorientation transition from the easy-plane type AFM to the easy-axis type AFM shown in the inset on the left side of Fig. 1(b).

To further corroborate the easy-axis type AFM order at low temperatures, we also performed polarized neutron scattering measurement at the POlarized Neutron Triple-Axis spectrometer PONTA installed at Japan Research Reactor 3. Similarly to the experiment at HRC, the (*H*,*H*,*L*) horizontal scattering plane was selected. We measured polarized neutron scattering profile of the 112 reflection at 100 K. The polarization direction of the incident neutron beam was set to be parallel to the vertical direction. As shown in Fig. 2, we observed a strong spin-flip (SF) scattering, which arises from the Fourier-transformed magnetization perpendicular to both the scattering vector and the vertical direction, in addition to a non-spin-flip (NSF) scattering, which includes the nuclear scattering. By combining the results from HRC and PONTA, we confirmed that the system exhibits the q=0 AFM structure with magnetic moments parallel to the *c* axis at low temperature.

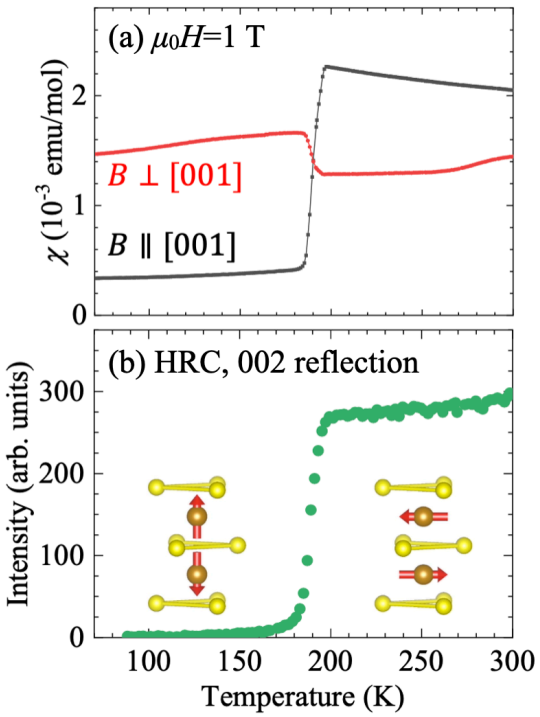

Fig. 1. (a) Temperature variations of magnetic susceptibility parallel and perpendicular to the c axis in FeS. (b) Temperature dependence of the integrated intensity of the 002 reflection measured at HRC in MLF of J-PARC.

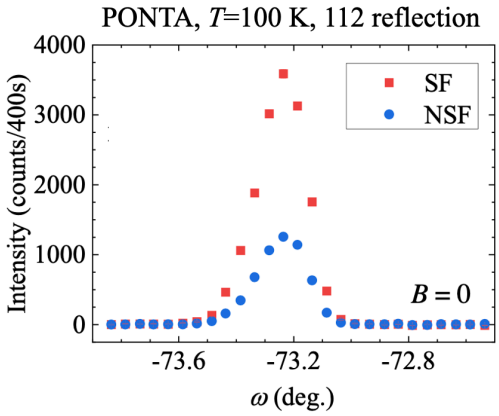

Fig. 2. Polarized neutron scattering profile of 112 reflection of FeS measured at 100 K.

References

[1] L. Šmejkal *et al*., Phys. Rev. X 12, 031042 (2022).
[2] R. Takagi *et al*., Nat. Mater. **24**, 63-68 (2024).

Authors

S. Seki[a], R. Takagi, A. Kitaori[a], H. Saito and T. Nakajima
[a]The University of Tokyo

PI of Joint-use project: S. Seki
Host lab: Neutron Science Laboratory

Gapless Magnon-Driven Anomalous Hall Conductivity in the Collinear Kagome Antiferromagnet $YbFe_6Ge_6$

$YbFe_6Ge_6$ is a kagome-lattice intermetallic whose Fe^{3+} moments order antiferromagnetically below $T_N \approx 500$ K. Neutron diffraction shows an A-type structure with spins along the c axis above the spin-reorientation temperature $T_{SR} \approx 63$ K; on cooling the moments rotate into the kagome plane while the propagation vector remains $\mathbf{k} = (0, 0, 0)$, preserving inversion–time-reversal symmetry and eliminating static scalar chirality [1]. Magnetotransport reveals that this reorientation generates an anomalous Hall conductivity $\Delta\sigma_{xy} \approx 30\ \Omega^{-1}\,cm^{-1}$ at 10 K for in-plane fields, whereas no signal appears for out-of-plane fields or $T > T_{SR}$, confirming its anisotropy dependence rather than any coupling to net magnetization [1].

Low-energy spin dynamics were resolved by inelastic neutron scattering. As shown in Fig. 1(a) [1], magnetic intensity at $\mathbf{Q} = (0, 0, 1)$ in the spin-reoriented phase is continuous up to ≈ 0.6 meV, defining a gapless magnon branch above the 0.14 meV resolution. The temperature evolution of intensities at 0.55 meV and 2.55 meV, plotted in Fig. 1(b) [1], demonstrates that the gap remains closed throughout the easy-plane phase and reopens abruptly at TSR, growing to 1.34 meV by 80 K. The concomitant loss of $\Delta\sigma_{xy}$, reproduced in Fig. 1(c) [1], shows a one-to-one correspondence between gapless magnons and Hall response: whenever the sub-meV continuum vanishes, the transverse conductivity collapses. A 7 T field also quenches $\Delta\sigma_{xy}$; its Zeeman energy for the 1.5 μ_B Fe moment is 0.6 meV, matching the upper edge of the gapless band and reinforcing the causal link.

Because the combined space inversion and time-reversal (*IT*) symmetry eliminates equilibrium Berry curvature and the magnetization never exceeds 0.3 μ_B/Fe even at 50 T, conventional intrinsic or skew-scattering mechanisms are excluded. Instead, propagating magnons transiently cant neighboring Fe moments; coupling to partially polarized Yb^{3+} spins biases the distribution of local scalar chiralities, creating a net dynamic Berry phase that deflects itinerant electrons. When the magnon gap opens thermally or via Zeeman splitting these fluctuations are suppressed and the Hall signal disappears [2]. Comparable fluctuation-driven Hall effects in kagome ferromagnets AMn_6Sn_6 [3] and in Fe_3Sn_2 [4] require non-collinear ground states, yet $YbFe_6Ge_6$ shows that collinear antiferromagnets can host the same physics provided that low-energy magnons are gapless. The absence of any Hall signal in FeSn, whose gap stays near 2 meV at all temperatures, underscores the necessity of near-zero-energy modes [5]. Only the quasi-acoustic branch softens across TSR; higher-energy magnons up to 40 meV remain unchanged, indicating that anisotropy rather than exchange drives the soft mode. Integrating the inelastic intensity yields a fluctuating Fe moment of $\approx 1.5\ \mu_B$, consistent with diffraction and validating the local-moment picture.

These results demonstrate that centrosymmetric, magnetically compensated antiferromagnets can exhibit field-controllable topological transport when anisotropy collapses the magnon gap to zero, extending antiferromagnetic spintronics beyond systems with static chirality and suggesting that engineered soft-mode transitions could enable chirality-mediated charge–spin conversion at terahertz frequencies [6].

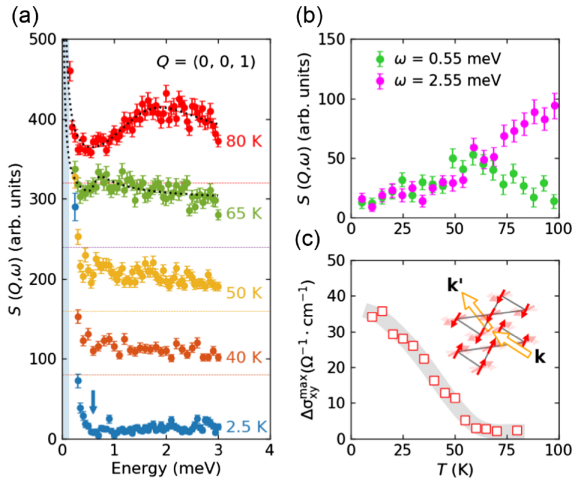

Fig. 1. (a) Low-energy spin excitations at (0, 0, 1) at selected temperatures, offset for clarity. Horizontal dashed lines indicate the zero intensity for the data above 2.5 K. Dashed curves are the fits to 65 K and 80 K data [36]. The light blue region shows energy resolution, and the arrow marks 0.6 meV, below which gapless excitations emerge. (b) Temperature dependence of the intensities at (0, 0, 1) at 0.55 meV and 2.55 meV. (c) Temperature dependence of the maximum magnitudes of $\Delta\sigma_{xy}$. The bold gray curve is a guide to the eyes. Inset illustrates electron scattering by the spin fluctuations.

References

[1] W. Yao *et al.*, Phys. Rev. Lett. **134**, 186501 (2025).
[2] W. Wang *et al.*, Nat. Mater. **18**, 1054 (2019).
[3] N. Ghimire *et al.*, Sci. Adv. **6**, eabe2680 (2020).
[4] M. Kang *et al.*, Nat. Mater. **19**, 163 (2020).
[5] S.-H. Do *et al.*, Phys. Rev. B **105**, L180403 (2022).
[6] Y. Fujishiro *et al.*, Nat. Commun. **12**, 317 (2021).

Authors

W. Yao[a,b], S. Liu[b] H. Kikuchi, H. Ishikawa, Ø. S. Fjellvåg[c,d], D. W. Tam[c], F. Ye[e], D. L. Abernathy[e], G. D. A. Wood[f], D. Adroja[f,g], C-M. Wu[h], C-L. Huang[i], B. Gao[a], Y. Xie[a], Y. Gao[a], K. Rao[a], E. Morosan[a], K. Kindo, T. Masuda, K. Hashimoto[b], T. Shibauchi[b], and P. Dai[a]

[a]Rice University, [b]The University of Tokyo, [c]Paul Scherrer Institut, [d]Institute for Energy Technology, [e]Oak Ridge National Laboratory, [f]Rutherford Appleton Laboratory, [g]University of Johannesburg, [h]National Synchrotron Radiation Research Center, [i]National Cheng Kung University

PI of Joint-use project: P. Dai
Host lab: Masuda Group and Kindo Group

Visualization of Electrically Controllable Magnetic Domains in a Quasi-One-Dimensional Quantum Antiferromagnet $BaCu_2Si_2O_7$

Quasi-one-dimensional quantum antiferromagnets (q1D-QAFMs) consist of chains of magnetic ions with a small spin quantum number (S = 1/2 and 1), where intrachain antiferromagnetic (AF) interactions dominate over interchain ones. They have attracted attention for their potential to exhibit exotic phenomena and their possible application in quantum spintronic technology. Like other AFMs, q1D-QAFMs will form a pair of domain states when undergoing an AF transition due to interchain interactions, typically represented by an "up-down-up-down" state and a "down-up-down-up" state. These domains are randomly distributed in a single crystal sample, and their observation and control are critical for device applications. However, observing domain patterns in q1D-QAFMs appears to be challenging because of the absence of net magnetization and strong quantum fluctuations reducing the ordered spin components. Indeed, there has been no experimental observation of the domain pattern in q1D-QAFMs.

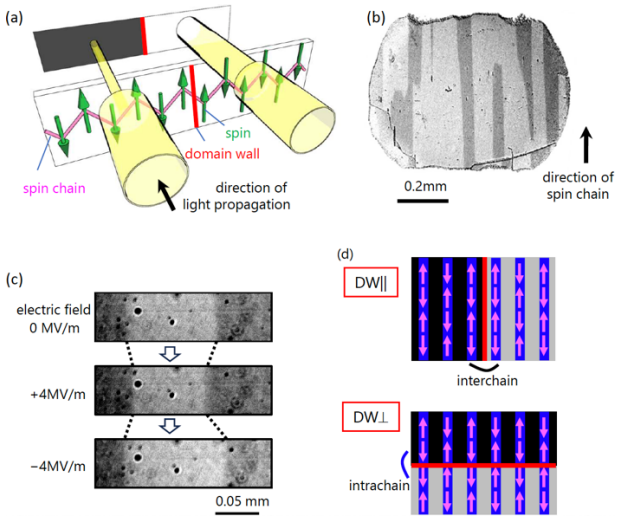

Fig. 1. (a) Schematic illustration of visualizing AF domains in a q1D-QAFM via NDD. Yellow transparent cylinders denote light beams along the thick black arrow, with diameter indicating intensity. In the AF phase, spins or magnetic moments (green arrows) are antiparallel, though parallel alignment can appear as a defect called a domain wall (red line). (b) Optical microscopy image of a sample at 5 K. (c) Visualization of electric-field-driven displacement of AF domain walls. (d) Schematics of a domain wall parallel (DW||) and perpendicular (DW⊥) to the spin chains.

In this study [1], we successfully visualize AF domains in one of the most representative spin-1/2 q1D-QAFMs, $BaCu_2Si_2O_7$, which orders antiferromagnetically below T_N = 9.2 K with reduced moments of only 0.1 μ_B per Cu^{2+} ion [2]. We use a recently developed optical imaging technique based on nonreciprocal directional dichroism (NDD) [3], a change in optical absorption upon reversing the light propagation direction or the sign of magnetic order parameters. Thus, AF domain patterns appear as differences in transmitted light intensity, as illustrated in Fig. 1(a). NDD requires breaking both space-inversion and time-reversal symmetries, which in $BaCu_2Si_2O_7$ arises from AF order combined with the zigzag chain arrangement of Cu^{2+} ions. We used single crystals of $BaCu_2Si_2O_7$ grown by the Masuda group using a floating zone method.

Figure 1(b) shows an optical microscopy image of a thin plate sample at 5 K below T_N. A clear two-level contrast appears in the AF phase, indicating the coexistence of the opposite AF domains. The image reveals that the domain walls (DWs) separating opposite AF domains run predominantly along the spin chains. After heating above T_N and cooling, the domain pattern was changed but the DW orientation was maintained, indicating the robust DW anisotropy in $BaCu_2Si_2O_7$. Furthermore, the AF domains can be controlled by an applied electric field with a small bias magnetic field. As highlighted by the dotted lines in Fig. 1(c), positive and negative electric fields shift the DWs in opposite directions. This displacement can be explained by a magnetoelectric coupling allowed by broken space-inversion and time-reversal symmetries. Importantly, the direction of the DWs is maintained during the displacement. Thus, the DW anisotropy also governs the electric-field driven DW motion in $BaCu_2Si_2O_7$.

Qualitatively, the observed DW anisotropy can be attributed to the anisotropic magnetic interactions. Figure 1(d) schematically shows spin arrangements near DWs parallel (DW||) and perpendicular (DW⊥) to the spin chains. The formation of DW⊥ costs the energy from strong intrachain interaction, which is two orders of magnitude larger than the interchain interactions governing DW||, making DW|| favorable, consistent with experiment. However, the interaction anisotropy greatly exceeds the DW anisotropy estimated by the ratio their lengths: $L_{DW||}/L_{DW\perp} \sim 10$. This suggests another factor contributes to the DW formation. To our knowledge, no relevant theory exists, and future work is required to clarify the microscopic origin of the DW anisotropy in the q1D-QAFMs.
In conclusion, this study advances understanding of domain physics of q1D-QAFMs and raises the interesting question of whether the domain pattern in $BaCu_2Si_2O_7$ is material-specific or intrinsic to q1D-QAFMs.

References

[1] M. Moromizato T. Miyake, T. Masuda, T. Kimura, and K. Kimura, Phys. Rev. Lett. **133**, 086701 (2024).
[2] M. Kenzelmann *et al*., Phys. Rev. B **64**, 054422 (2001).
[3] K. Kimura *et al*., APL Mater. **11**, 100902 (2023).

Authors

K. Kimura[a]
[a]Osaka Metropolitan University

PI of Joint-use project: Kenta Kimura
Host lab: Masuda Group

Tough and Elastic Ion Gels Reinforced by Strain-Induced Crystallization

Ion gels, containing a polymer network and an ionic liquid as their solvent, are deemed one of the most promising soft materials for stretchable electronics, which may supersede incumbent rigid wearable devices in the future. Developing tough ion gels is indispensable for applications, including, but not limited to, conformal wearables or soft actuators. One of the mainstream strategies for materializing tough gels is introducing a sacrificial polymer network. Therein, noteworthy work includes that of double-network (DN) hydrogels [1], and successful fabrication of tough DN or self-healing ion gels followed. However, the very nature of the "sacrificial" network in those gels deteriorates their instantaneous mechanical reversibility. Aiming to overcome this shortcoming, we turned to strain-induced crystallization (SIC, Fig. 1) in gels. Although SIC itself is a long-renowned reinforcement mechanism within vulcanized natural rubber or certain types of polymers, it proved equally valid in polymer gels, which was found in slide-ring (SR) hydrogels of a high polymer concentration and a high molecular weight between cross-links [2]. We implemented this SIC strategy for fabricating tough ion gels. In this presentation, we will overview scattering patterns of in-situ wide-angle X-ray scattering (WAXS), small-angle X-ray scattering (SAXS), and small-angle neutron scattering (SANS) obtained from the ion gels being stretched, and discuss what is inferred about the structural deformation of the polymer network therein. We will also discuss the paths to designing an ion gel of better mechanical performance, from the results of the complementary scattering experiments.

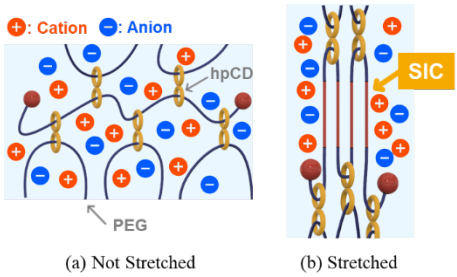

Fig. 1. SIC of highly exposed and oriented PEG chain(s) in an SR ion gel. SIC is formed when the gel is stretched beyond its threshold strain, and it disappears as soon as the load is removed.

We fabricated SR ion gels, in which polyrotaxane (PR) supramolecules possess dynamic crosslinking points via their ring-shaped molecules. The PR was comprised of the axial component, polyethylene glycol (PEG), and the annular ones, (2-hydroxypropyl)-α-cyclodextrin (hpCD). We used an imidazolium-based ionic liquid, 1-ethyl-3-methylimidazolium bis(trifluoromethanesulfonyl)imide ([C2mim][NTf2]), as their solvent. Since [C2mim][NTf2] has an X-ray scattering length density close to that of hpCD, the SAXS patterns reflected the contrast derived from PEG, suppressing the one from hpCD. On the other hand, no contrast matching was realized in the gels for in-situ SANS between the three constituents: deuterated [C2mim][NTf2]-d_8, PEG, and hpCD. SANS measurements were performed at SANS-U, JRR-3.

At a large strain (λ = 10, λ represents the extension ratio), as shown in Fig. 2, scattering spots corresponding to the planar zigzag crystalline structure of PEG were confirmed in the WAXS patterns, and a vertical streak perpendicular to the stretching direction was identified in SAXS, which we concluded as an indication of highly oriented PEG. The SANS patterns suggests that hpCDs form aggregations and that the aggregates are deformed by stretching [3].

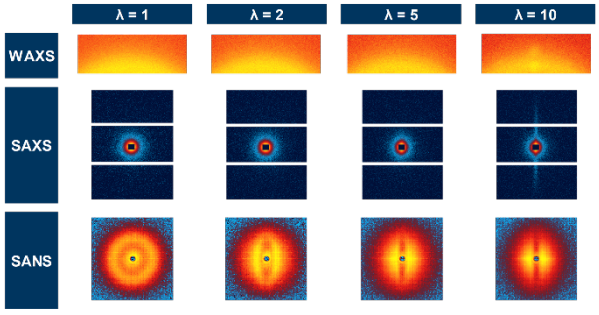

Fig. 2. In-situ WAXS, SAXS, and SANS patterns from SR ion gels being stretched in the horizontal direction.

References

[1] J.P. Gong, Y. Katsuyama, T. Kurokawa, Y. Osada., Adv. Mater., **15**, 1155 (2003).
[2] C. Liu, N. Morimoto, L. Jiang, S. Kawahara, T. Noritomi, H. Yokoyama, K. Mayumi, and K. Ito., Science, **372**, 1078 (2021).
[3] T. Enoki, K. Hashimoto, T. Oda, K. Ito, and K. Mayumi, Macromolecules, **57**, 11498 (2024).

Authors

K. Mayumi, T. Enoki, and K. Hashimoto[a]
[a]Gifu University

PI of Joint-use project: K. Hashimoto
Host lab: Neutron Science Laboratory

Observation of The Mexican Hat–Shaped Valence Band of ferroelectric α-In_2Se_3

This study investigates the electronic band structure of the van der Waals ferroelectric semiconductor α-In_2Se_3 using nanoscale angle-resolved photoemission spectroscopy (ARPES), magneto-optical transmission under high magnetic fields up to ~60 T, and Density Functional Theory (DFT) [1]. These experiments reveal that α-In_2Se_3 hosts an indirect band gap and a distinctive inverted Mexican hat–shaped (IMH) valence band - featuring a nearly flat central region surrounded by a hexagonal ring of maxima and saddle points. This topology results in van Hove singularities and large hole effective masses, validating long-standing theoretical predictions.

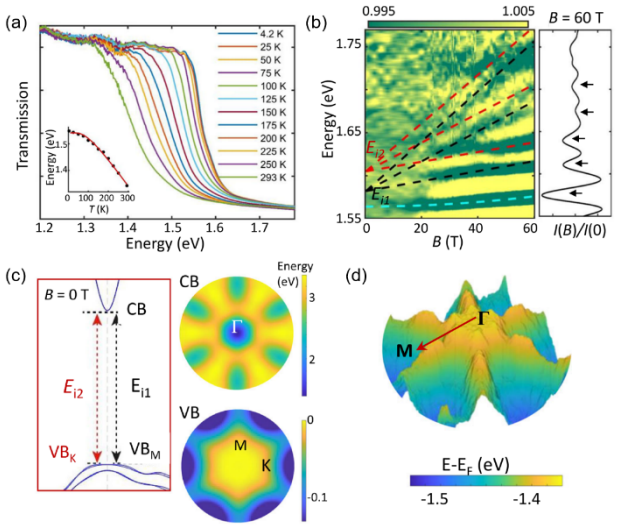

Fig. 1 (a) Temperature-dependent transmission spectra of α-In_2Se_3. Insert: band gap energy as a function of temperature fitted by an empirical model. (b) Color plot of magneto-transmission spectra of α-In_2Se_3 with magnetic field up to 60 T. (b) Electronic band structure of α-In_2Se_3 calculated from DFT. (d) Energy dispersion of α-In_2Se_3 as measured by ARPES for the uppermost valence band.

Figure 1 highlights the temperature and magnetic field dependent optical properties of α-In_2Se_3. At zero magnetic field, the transmission spectra (Fig. 1(a)) exhibit a clear blue shift in the indirect absorption edge from 1.35 eV at 293 K to 1.54 eV at 4.2 K. These values align well with previous reports [2-3] despite prior claims that α-In_2Se_3 exhibits a direct band gap [3-4]. An inset in Fig. 1(a) shows the temperature dependence of the band gap energy, fitted by an empirical model that commonly applies to indirect band gap semiconductors. This excellent agreement reinforces the assignment of α-In_2Se_3 to an indirect band gap semiconductor.

Figure 1(c) presents the magneto-transmission spectra at $T = 4.2$ K, normalized to zero field spectrum ($I(B)/I(0)$). At high field (~60 T), five distinct absorption features emerge. The lowest-energy feature is attributed to an excitonic transition, whose diamagnetic shift is well described using a binding energy of 18 meV and a shift coefficient σ = 3.3 μeV/T². The higher-energy features correspond to two sets of interband Landau level transitions: one from the valence band maximum located at the M-point, and another from a saddle point in the K-point of the valence band, denoted as E_{i1} (black) and E_{i2} (red) in Fig. 1(c). The extracted effective reduced masses ($\mu \approx 0.11\ m_e$) and energy separations (ΔE_i = 23 meV) are in excellent agreement with ARPES (Fig. 1(d)) and DFT results, confirming the IMH-like valence band structure.

The evolution of the interband optical transitions with magnetic field provides direct experimental access to the effective mass and band-edge topology, consistent with the features predicted by DFT calculations. These optical signatures serve as a fingerprint of the complex valence band landscape and illustrate the power of magneto-optical spectroscopy in mapping electronic structures in layered van der Waals semiconductors.

These results validate theoretical predictions about IMH bands in layered semiconductors. The combination of ferroelectric behavior and tunable electronic structure opens possibilities for engineering van der Waals devices—such as low-power, memory, and neuromorphic systems—by tailoring band topology, carrier mass, and density of states.

References

[1] J. Felton *et al.*, Nature Communications **16**, 922 (2025).
[2] J. Quereda *et al.*, Adv. Optical Mater. **4**, 1939 (2016).
[3] M. Emziane *et al.*, Mater. Chem. Phys. **62**, 84 (2000).
[4] G. Kremer *et al.*, ACS nano **17**, 18924 (2023).

Authors

Z. Yang, A. Patanè[a], and Y. Kohama
[a]University of Nottingham

PI of Joint-use project: A. Patanè
Host lab: Kohama Group

Magnetic Shape Memory Effect in a Heavy-Fermion System $CeSb_2$

"Magnetic shape memory effect", the phenomenon that deformed materials returning to their original shape upon exceeding a certain magnetic field, can be adopted for applications such as field-tuned actuators, as it offers much faster controllability than the temperature-driven shape memory effect. The magnetic shape memory effect has been studied predominantly in Heusler alloys composed of transition metals using magnetic and structural properties of martensitic and parent phases. Similar effects are well studied for the *f*-electron compounds RCu_2 (*R*: rare-earth elements) [1]. Applying a magnetic field along the hard magnetization axis causes a rapid increase in magnetization that results in the direction of the field becoming the easy magnetization axis. However, such memory effects in RCu_2 are stable only at low temperatures, and no *f*-electron compounds that maintain memory at room temperature have been identified. This study revealed that the heavy-fermion compound $CeSb_2$ exhibited easy-axis switching accompanied by crystal-axis conversion under a magnetic field. Remarkably, this magnetic shape memory effect remains stable, even at room temperature.

As shown in Fig. 1(a), $CeSb_2$ exhibits a sharp metamagnetic-like increase in magnetization near 34 T, and significant hysteresis is observed during demagnetization when a magnetic field is applied along one of the in-plane principal axes [2]. Subsequent measurements revealed a memory effect, that is, the magnetization approached its previous maximum. The measurements obtained by applying fields along the other in-plane axis revealed a reduction in magnetization, indicating that the direction perpendicular to the field becomes the hard axis. These observations were surprising because the applied field direction was changed by rotating the sample by 90° after heating the sample to room temperature. Moreover, the change from the hard to easy axis is reproducibly observed through the higher-field magnetization measurements. These findings demonstrate that the "magnetic memory effect" remains stable up to at least room temperature. This easy-axis switching accompanies crystallographic axis conversion, which can be confirmed as a domain rearrangement through a polarizing light microscope. Thus, this phenomenon constitutes a "magnetic shape memory effect" that is remarkably stable at room temperature.

$CeSb_2$ crystallizes in a nearly tetragonal orthorhombic lattice that consists of Sb layers and Ce-Sb layers stacked along the orthorhombic *c*-axis. Ce atoms in the *ab*-plane form a distinctive "pantograph" structure [Fig. 2]. Adjusting the pantograph angles allows the lattice constants to be swapped between the *a*- and *b*-axes. The Sb_2 sandwiched between the Ce pantographs forms dimers and acts as hinges during axis transformations. The magnetic anisotropy inherent in the pantograph structure is a key to the magnetic shape memory effect of $CeSb_2$.

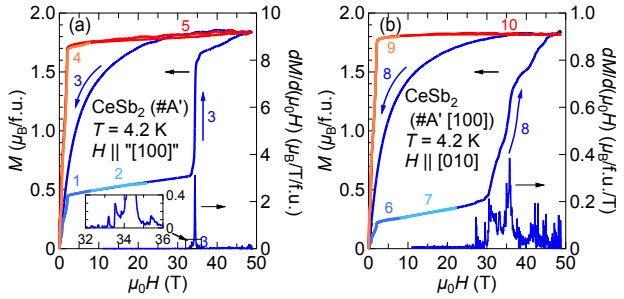

Fig. 1. (a) Magnetization [M (H)] curves of the as-cast $CeSb_2$ (#A') at 4.2 K by applying the fields along one of the in-plane axes. (b) M (H) curves measured at 4.2 K after rotating the same sample 90° at room temperature to change the applied field direction. The number indicates the order of measurements.

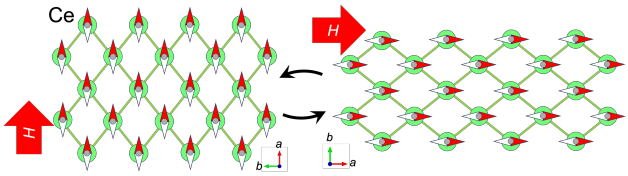

Fig. 2. Schematic drawing of the Ce-pantograph network. By changing the field direction, the pantograph angles change accompanied by the easy-axis switch.

Although the relationships between the magnetic shape memory effect and heavy electron states remain unclear, the characteristic feature of $CeSb_2$, which memorizes the magnetization values corresponding to the maximum applied field, indicates its potential as a magnetic memory material. This discovery opens new avenues for exploring materials for practical applications under moderate magnetic fields and temperatures.

References

[1] see for example, K. Sugiyama *et al.*, J. Magn. Magn. Mater. **262**, 389 (2003).
[2] A. Miyake *et al.*, J. Phys. Soc. Jpn. **94**, 043702 (2025).

Authors

A. Miyake[a], R. Hayasaka[a], H. Fukuda[a], M. Kondo, Y. Kinoshita, D. Li[a], A. Nakamura[a], Y. Shimizu[a], Y. Homma[a], F. Honda[b], M. Tokunaga, and D. Aoki[a]
[a]IMR, Tohoku University
[b]RI center, Kyushu University

PI of Joint-use project: A. Miyake
Host lab: Tokunaga Group

Photo-Induced Nonlinear Band Shift and Valence Transition in SmS

Strongly correlated materials near quantum criticality show unique phase transitions—metal-insulator, magnetic to nonmagnetic—when pressure or magnetic fields are applied. Recently, photo-excitation has emerged as a tool to create nonequilibrium states, including transient metallic [1] and superconducting phases [2], with potential applications in ultrafast electronics. SmS, a black semiconductor at ambient conditions, transitions to a golden semimetallic state above 0.65 GPa via a Sm^{2+} to Sm^{3+} valence change. Optical excitation may mimic this phase by generating electron–hole pairs, offering a new pathway to study valence dynamics. Time-resolved ARPES (TrARPES) enables visualization of such transient states, having revealed phenomena like Floquet–Bloch states [3] and excitonic transitions [4].

Figures 1(a) and 1(b) show an angle-resolved photoelectron spectroscopy (ARPES) image and the corresponding angle-integrated photoelectron (AIPE) spectrum. The three peaks at approximately 1, 1.7, and 2.5 eV indicated by dashed lines in Fig. 1(d) are the Sm 4f multiplets of bulk-6H [6H(b)], the overlap of bulk-6F [6F(b)] and surface-6H [6H(s)], and surface-6F [6F(s)], respectively.

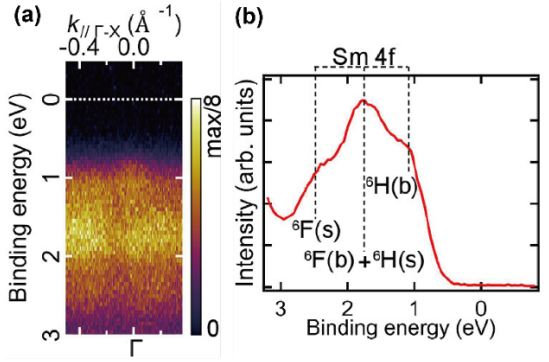

Fig. 1. (a) Band mappings of SmS with ARPES without the photo-irradiation of a pump laser. (b) Angle-integrated-photoelectron spectrum of (a). The multiplet structures of the Sm^{2+} $4f^5$ final state are visible. The peak positions of Sm $4f^5$ multiplets are indicated by the dashed lines

The colored solid lines in Fig. 2(a) labeled as different fluences show the AIPE spectra of the multiplet structure of the Sm^{2+} $4f^5$ final state, obtained immediately after the arrival of the pump pulse. Meanwhile, the spectrum obtained immediately before the arrival of the pump pulse is shown as a black dashed line. After photo-irradiation, the spectrum shifts toward low binding energies but in the opposite direction to the shift at $\Delta t < 0$, that is, a nonlinear shift in time. To investigate the time development of the energy shift after photo-irradiation, the spectra were fitted by the same procedure mentioned above, and the peak shift was plotted as a function of delay time, as shown in Fig. 2(b). The AIPE spectrum shifts towards the Fermi level within 0.1 ps and then gradually shifts back in the following several picoseconds to the position before pumping.

To obtain a more quantitative understanding, we fitted the time-dependent energy shift to a single-exponential decay function convoluted with a Gaussian function, as shown in Fig. 2(b). The fitting parameters, that is, the maximum energy shift (E_{smax}), recovery time τ, and rise time τ_r at different pump fluences, are plotted as functions of the pump fluence in Figs. 2(c)–2(e). Figure 2(c) shows the pump fluence dependency of E_{smax}. E_{smax} initially increases as fluence increases up to a pump fluence of approximately 1.2 mJ/cm^2 and then saturates at a certain value. The saturation value of E_{smax} was evaluated as 58 ± 4 meV by assuming a single-exponential function. The recovery time τ and rise time τ_r are shown in Figs. 2(d) and 2(e), respectively. Both parameters remained constant at each fluence; τ was as long as 1 ps, and τ_r was several tens of femtoseconds, which is comparable to the time resolution.

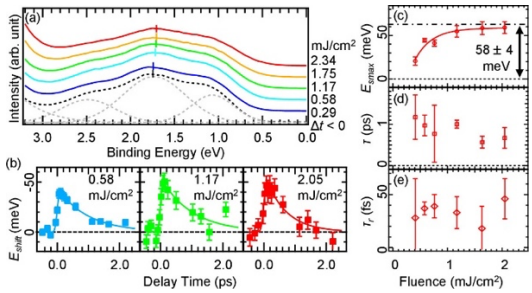

Fig. 2. (a) AIPE spectra of the multiplet structure of SmS 4f final state before the arrival of the pump pulse ($\Delta t < 0$) (black dashed line) and just after the arrival of the pump pulse (less than 0.1 ps) under irradiation of the pump laser with a fluence. (b) Time structure of the energy shift of the three 4f multiplet peaks at various pump fluences. (c) Pump fluence dependence of the maximum energy shift of the 4f multiplet structure at $\Delta t > 0$. (d) Relaxation time of the fitting function in (b) as a function of pump fluence. (e) Energy shift time after photo-irradiation as a function of pump fluence.

The Sm 4f band shifts upward rapidly and soon shifts back within several ps. Photo-induced band narrowing, SPV shift, or heating effect of the pump pulse are possible candidates to explain this ultra-fast band shift. However, this band shift happens in ps, which is much faster than the excitation of the thermal phonons. Therefore, the photo-induced band shift seems to be the most possible scenario.

References

[1] K. Miyano *et al*., Phys. Rev. Lett. **78**, 4257 (1997).
[2] A. Cavalleri, Contemp. Phys. **59**, 31 (2018).
[3] Y. H. Wange *et al*., Science **342**, 453 (2013).
[4] K. Okazaki *et al*., Nat. Commun. **9**, 4322 (2018).

Authors

Y. Chen[a], T. Nakamura[a], H. Watanabe[a], T. Suzuki, Q. Ren, K. Liu, Y. Zhong, T. Kanai, J. Itatani, K. Okazaki, H. S. Suzuki, S. Shin[b], K. Imura[c], N. K. Sato[d], and S. Kimura[a]
[a]The University of Osaka
[b]The University of Tokyo
[c]Nagoya University
[d]Aichi Institute of Technology

PI of Joint-use project: T. Nakamura
Host lab: Okazaki Group